Supporting Information: Two-Photon Photoluminescence Excitation Spectra of Perovskite Nanocrystals in Glass Matrix†

M. N. Bataev,*,‡ I. V. Ignatiev,‡ E. V. Ubyivovk,¶ D. V. Pankin,§ M. B. Smirnov,§ M. S. Kuznetsova,‡ and E. V. Kolobkova‖,⊥

‡*Spin Optics Laboratory, St. Petersburg State University, 198504 St. Petersburg, Russia*

¶*St. Petersburg State University, 198504 St. Petersburg, Russia*

§*Department of Solid State Physics, St. Petersburg State University, 198504 St. Petersburg, Russia*

‖*ITMO University, 199034 St. Petersburg, Russia*

⊥*St. Petersburg State Institute of Technology, 190013 St. Petersburg, Russia*

E-mail: batae1996@gmail.com

S1 Experimental methods

Optical characterization (transmission and PL spectra):

The PL and transmission spectra were measured using the same optical setup as in the 1P-PLE and 2P-PLE experiments. For transmission measurements, broadband light from the halogen–tungsten lamp was passed through a spectral filter to suppress spectral components

†A footnote for the title

capable of exciting PL in the nanocrystals. The filtered beam was transmitted through the sample, which remained mounted inside the closed-cycle helium cryostat at 10–12 K. The transmitted light was collected and analyzed using the same M522 spectrograph and Hamamatsu CCD array.

For PL measurements, continuous-wave (CW) diode lasers with photon energies of 3.06 eV and 2.33 eV were used as excitation sources. The PL emission was collected in backscattering geometry and recorded under the same conditions as in the PLE measurements.

X-ray diffraction spectra:

The precipitation of NCs in FP glass was confirmed using X-ray diffraction (XRD) method. Diffraction patterns were recorded with Rigaku X-ray diffractometer equipped with Cu K_α radiation. The X-ray diffraction was detected in the double angle range from 10 ° to 80 degrees ° in the Bragg-Brentano geometry. A 0.02-mm-thick Ni foil was applied to suppress Cu K_β radiation. The measurement step was 0.05 degree °. The identification was performed using PDWin 3.0 software package. The search of analogues was carried out within the ICDD PDF-2 database of powder X-ray diffraction patterns.

Transmission electron microscopy:

To determine the shape, average size, and size distribution of the NCs we employed the Zeiss Libra 200FE scanning transmission electron microscope (STEM). Due to the high resistivity of the glass, which caused charging under electron beam irradiation, special preparation was required prior to TEM imaging. The glass sample was ground into a fine powder using an agate mortar. The powder was dispersed in an ultrasonic bath to ensure proper separation of NCs. A drop of the suspension was deposited onto a carbon-coated copper grid for analysis.

S2 Sample Characterization

When working with perovskite materials, structural characterization of the samples is essential. Figure S1 shows XRD patterns of glasses containing $CsPbBr_3$, $CsPb(Cl,Br)_3$, and $CsPbI_3$ nanocrystals (NCs), plotted in blue, red, and green, respectively. To determine the composition of the synthesized nanocrystals, we recorded XRD patterns and used the positions of their characteristic peaks to estimate the average crystallite size via the Debye–Scherer formula.

The Scherrer equation can be written as $d = K\lambda/(\beta \cos\theta)$, where K is a dimensionless shape factor equal to 0.9; λ is the X-ray wavelength; β is the line broadening (full width at the half maximum, FWHM), in radians, θ is the Bragg angle. However, the NCs are present at low volume fractions ($\approx$ 1 vol.%) and precise size determination is not possible. Nevertheless, using the Debye-Scherer equation to each diffraction pattern,an approximate NC diameter was obtained to be of 13 ± 1 nm and 15 nm for the $CsPb(Cl,Br)_3$ NCs and $CsPbBr_3$ NCs, respectively. The determination of the size of $CsPbI_3$ NCs from the XRD spectra is impossible due to the relatively small content of the NCs in the glass matrix.

As it can be seen from the Figure S1, the position of the XRD peaks shifts when the composition changes from $CsPb(Br,Cl)_3 \rightarrow CsPbBr_3 \rightarrow CsPbI_3$, these peaks shift toward lower diffraction angles—reflecting the increase in lattice constant. The patterns at such angles are characterized by the orthorhombic phase (JCPDS No. 01-072- 7929) of $CsPbBr_3$ NCs, (JCPDS No. 01-075- 0411) $CsPb(Br,Cl)_3$ and $CsPbI_3$ (JCPDS No 80-4039) NCs. The small concentration of NCs does not allow us to determine the perovskite phase accurately due to the coincidence of intense peaks of high (cubic) and low-temperature (orthorhombic) phases.

The observed peaks in the X-ray diffraction patterns of the bromide NC and iodide NC completely coincide with the characteristic positions of single crystals, as given in the database. For the mixed NC, the peaks are located between the peaks of the chloride and bromide compositions, which allow estimating the ratio of chlorine to bromine in the NC

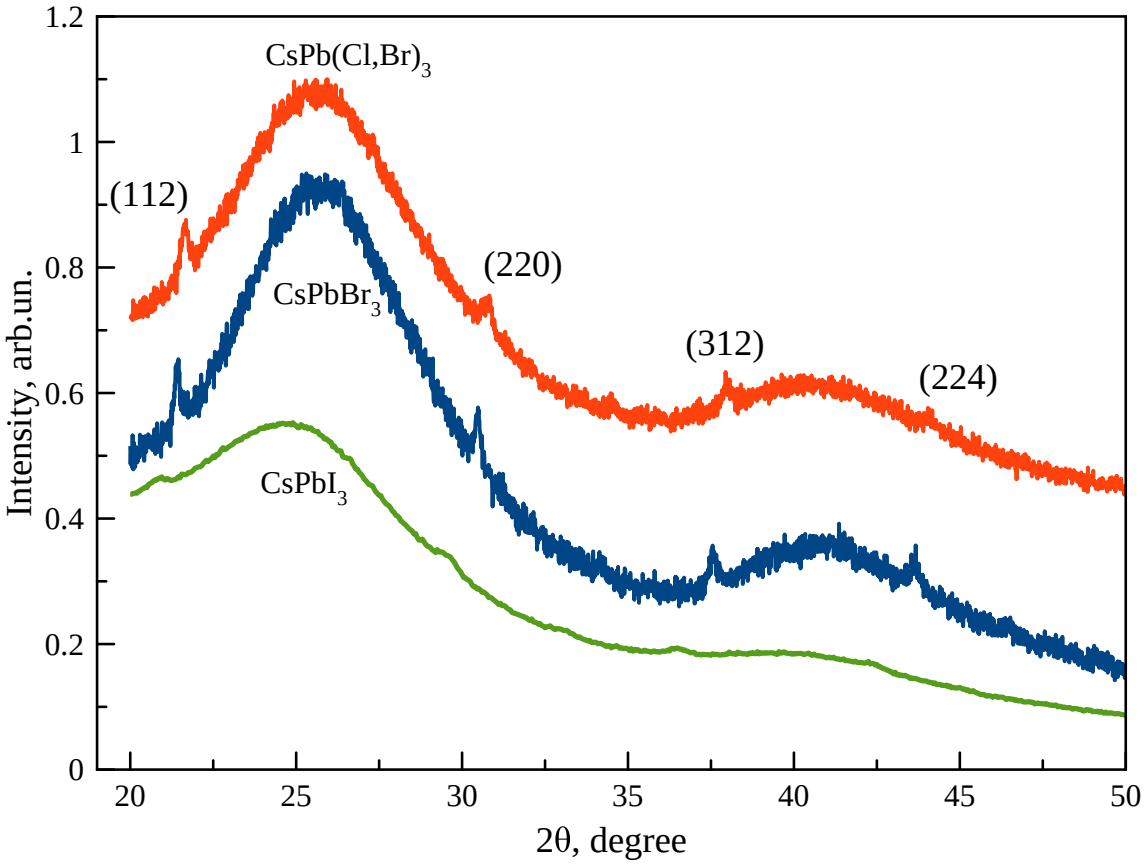

Figure S1: XRD patterns of the glasses doped with $CsPbBr_3$ (JCPDS No. 01-072- 7929), $CsPb(Br,Cl)_3$ (JCPDS No. 01-075- 0411) and $CsPbI_3$ (JCPDS No. 80-4039) NCs.

composition. It is known that, at room temperature, the stable crystalline phase for halide perovskites is the orthorhombic phase. Typically, in literature sources, when interpreting the peaks, the designations corresponding to the cubic phase are given, which for single crystals is stable above 405 K. Differences in the diffraction patterns of the two phases can be observed in the angular range of 30 to 35 degrees in the form of very low intensity peaks, which can only be detected for a high concentration of NCs, such as powders after colloidal synthesis. The low concentration of NCs in glasses does not allow the detection of low-intensity peaks. Thus, in the figure, the observed peaks should have different Miller indices corresponding to the gamma phase. They are as follows: (112), (220), (312), and (224).

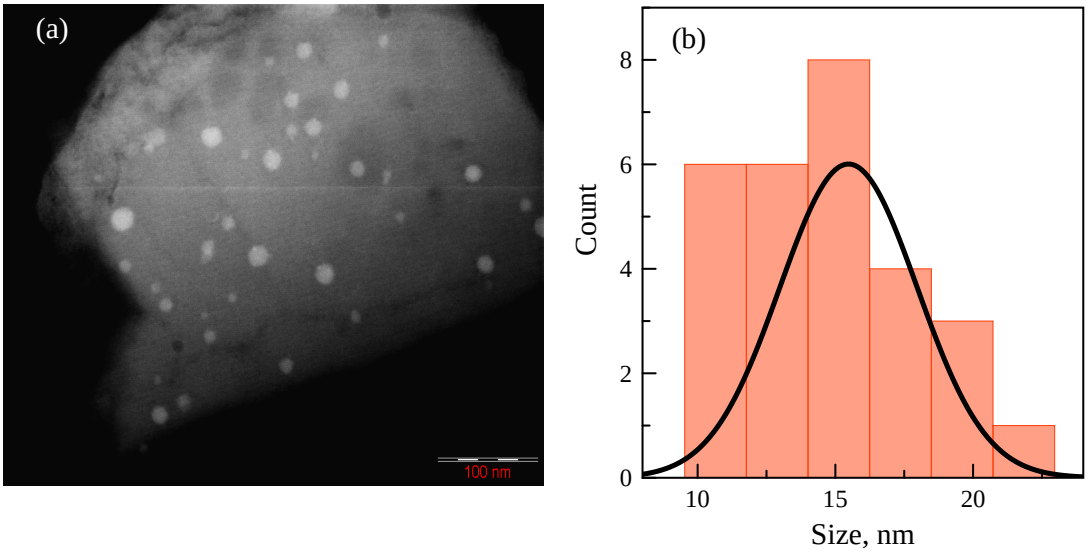

Figure S2: (a) TEM image of the glass containing $CsPbI_3$ NCs. The NCs are visible as white spots in the image. (b) statistical distribution of the NC diameter.

A more precise method for determining particle sizes is the transmission electron microscopy (TEM). Our nanocrystals are embedded in a glass matrix and, since glass is a dielectric material, obtaining TEM images becomes a complex and specialized task. Figure S2 (a) shows the TEM image for piece of the glass sample with the $CsPbI_3$ NCs. Using the calibrated ruler, we have obtained the histogram of the NCs sizes [Figure S2 (b)]. The average size of the NCs obtained from this histogram is (15.6 ± 2.5) nm. We should note that the average size of NCs is larger than the exciton Bohr radius. Correspondingly, the quantum

confinement effect does not contribute significantly to the energy shift of the lowest optical transitions. The information of the size and shape of the $CsPbBr_3$ and $CsPb(Br,Cl)_3$NCs can be found in Refs.[1,2]

S3 Optical characterization

After structural characterization, the next crucial step involves optical characterization of the studied samples. Figure S3 presents the measured PL spectra under one-photon and two-photon excitation as well as the corresponding transmission spectra for three types of perovskite NCs at cryogenic temperatures: (a) $CsPb(Br,Cl)_3$, (b) $CsPbBr_3$, and (c) $CsPbI_3$. The one-photon PL spectra were recorded at excitation photon energies of 3.06 eV for the samples with $CsPb(Br,Cl)_3$ and $CsPbBr_3$ NCs and 2.33 eV for the iodide-based sample. The PL bands have a full width at half maximum (FWHM) of 40 meV for the $CsPb(Br,Cl)_3$ NCs, 18 meV for$CsPbBr_3$, and 25 meV for $CsPbI_3$ NCs, respectively. Such narrow PL linewidth indicate a tight size distribution and high sample quality.

The two-photon PL spectra demonstrate the effect of spectral filtering of the PL from the sample volume. Namely, the high-energy wing of the PL band is suppressed due to the reabsorption of the PL excited by two photons in deep layers of the sample. This effect results in a specific profile of the two-photon PL band, in particular, for the $CsPbI_3$ NCs, see Fig. S3(c).

Transmission spectra (red curves) were measured under identical cryogenic conditions (T = 11 K) and provide complementary information on excitonic and interband absorption features. A typical transmission spectrum of the FP glass without NCs is shown in Figure S3(d) (blue line). This panel also shows a transmission spectrum of FP glass containing a non-luminescent "yellow" δ-phase of $CsPbI_3$ NCs (red line). We assume that this phase determines the transmission edge at lower energies of about 2.8 eV (red line) and is responsible for the decrease of the 1P-PLE signal $CsPbI_3$ NCs shown in Fig. 3(c).

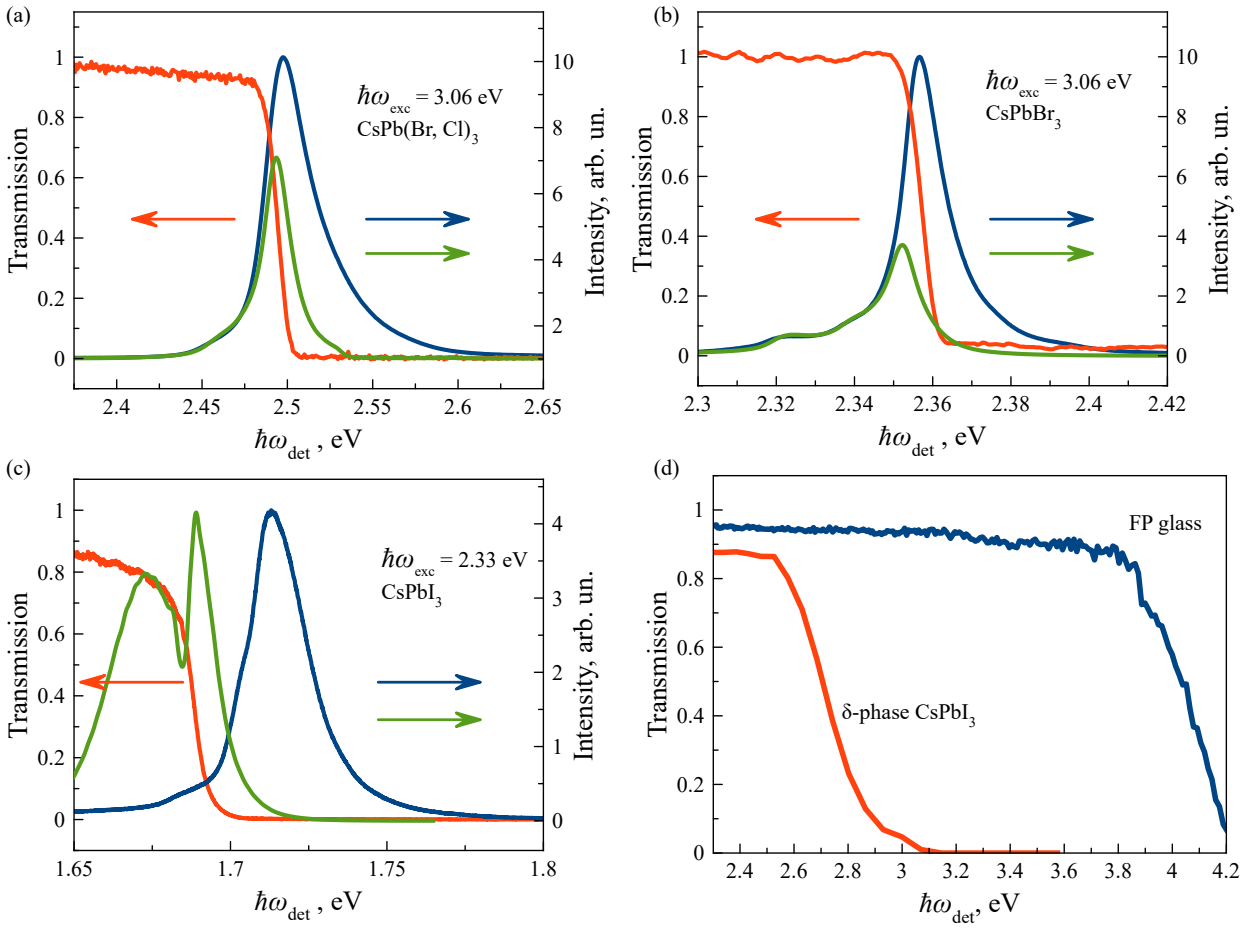

Figure S3: (a - c) PL spectra under one-photon (blue lines) and two-photon (green lines) excitation and corresponding transmission spectra (red lines) of (a) $CsPb(Br,Cl)_3$ NCs at $\hbar\omega_{exc} = 3.06$ eV, (b) $CsPbBr_3$ NCs at $\hbar\omega_{exc} = 3.06$ eV, and (c) $CsPbI_3$ NCs at $\hbar\omega_{exc} = 2.33$ eV. T = 11 K. (d) Transmission spectra of pure glass (blue line) and glass with $CsPbI_3$ NCs growth in δ-phase (red line). T = 290 K.

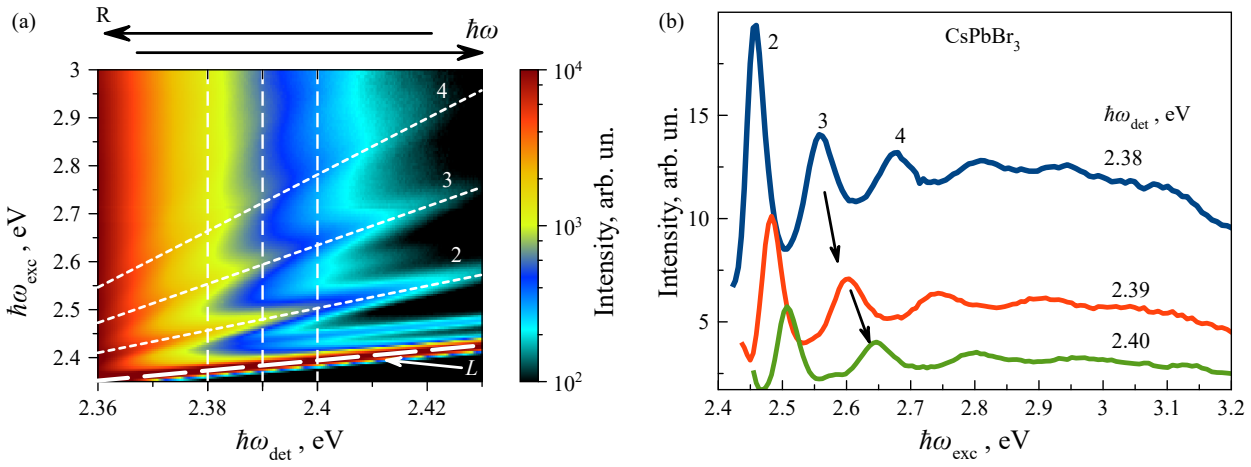

Figure S4: (a) Part of the 1P-PLE color map for the $CsPbBr_3$ NCs. (b) Examples of the PLE spectra obtained as the cross-sections of the color map at fixed PL detection energies shown by vertical dashed lines in (a). Tilted dashed lines show examples of the spectral dependencies of the quantum-confined exciton states.

In Figure S4(a) and (b), the PLE spectra under one-photon excitation are presented for $CsPbBr_3$ NCs. Spectral features corresponding to optical transitions to different quantum-confined exciton levels are clearly observed.[3] The energy spacing between the levels increases with decreasing the NC radius R and, correspondingly, increasing the PL photon energy. This results in the "fan"-like energy dependence of the levels.

S4 Two photon absorption coefficient

The two-photon absorption (TPA) coefficient β is investigated using two main methods, (i) the nonlinear optical imaging technique with a phase object (NIT–PO)[4–6] and (ii) so-called Z-scan technique.[7–9] The coefficients β measured in several works by the Z-scan method for perovskite $CsPbBr_3$ nanocrystals and quantum dots synthesized using different approaches are compared in Table 1. The magnitude of β strongly depends both on experimental parameters, such as the peak power per pulse, the pulse duration, and the pulse repetition rate, as well as on the parameters of the investigated system, including the nanocrystal size and their concentration. A table summarizing the obtained values of TPA coefficient for

perovskite materials with different chemical compositions and dimensionalities is also given in Ref.[10]

Table 1: Comparison of two-photon absorption coefficients (TPA coefficient, β) for perovskite nanocrystals measured under different experimental conditions. The laser pulse parameters: τ is the pulse duration, ν is the pulse repetition rate.

Perovskite	Laser parameters (τ, ν)	Excitation λ_{exc}, nm	Excitation power (GW/cm^2)	β (cm/GW)	Ref.
$CsPbBr_3$ NCs in fluorophosphate glass	150 fs, 80 MHz	800	3	0.63	This work
$CsPbBr_3$ NCs in borosilicate glass	226 fs, 1 kHz	1030	0.5–3 mW	0.032–0.185 (power dependence)	[11]
$CsPbBr_3$ NCs in toluene	100 fs, 1 kHz	800	20	0.097	[12]
$CsPbBr_3$ NCs in toluene	100 fs, 1 kHz	800	40–80	0.097	[13]
$CsPbBr_3$ NCs in hexane	130 fs, 76 MHz	800	1.5 / 0.1	1.71 (green) / 0.68 (blue)	[14]
$CsPbBr_3$ NCs	396 fs, 1 kHz	787	3 mW	0.0322	[15]
$CsPbBr_3$ NCs	70 fs, 1 kHz	800	90	0.039	[16]
$CsPbBr_3$ NCs	70 fs, 1 kHz	800	20	1.8	[17]
$CsPbBr_{2.7}I_{0.3}$ NCs	100 fs, 1 kHz	780	–	0.338	[18]

As can be seen from the table, with rare exceptions, the TPA coefficient for the $CsPbBr_3$ NCs embedded in a fluorophosphate glass matrix exhibits relatively high value. Further study of nanocrystals with different sizes and chemical compositions is required in order to systematize the understanding of the parameters affecting the magnitude of the TPA coefficient.

S5 DFT calculations

The band structure calculations were performed in order to determine the energy positions of spin-split electronic states in the orthorhombic phase of $CsPbI_3$. These values were subsequently used for comparison with experimental data to analyze the effect of spin-orbit coupling in this low-symmetry perovskite modification.

In order to perform the calculations, the Perdew–Burke–Ernzerhof (PBE) exchange-correlation functional within the generalized gradient approximation (GGA) of density functional theory (DFT)[19] was chosen. Dispersion interactions were accounted for using the Tkatchenko–Scheffler (TS) correction scheme,[20] resulting in the so-called TS-GGA-PBE theoretical approach. The calculations were carried out both with and without spin-orbit coupling (SOC). In the SOC-included case, a scissor operator of 0.96 eV was applied. A plane-wave cutoff energy of 1200 eV was used, and norm-conserving pseudopotentials[19] were employed. The self-consistent field (SCF) convergence criterion was set to 10^{-7} eV/atom. All calculations were performed using the CASTEP software package.[19,21] Prior to band structure calculations, structural optimization of the crystal geometry was carried out using the modified Broyden–Fletcher–Goldfarb–Shanno (LBFGS) algorithm.[22,23] The convergence criteria were: maximum atomic displacement less than 5×10^{-4} Å, residual stress below 0.02 GPa, and residual forces below 0.01 eV/Å. The Brillouin zone was sampled using the Monkhorst–Pack scheme[24] with a k-point spacing of 0.04 $Å^{-1}$. The electronic band structure was computed within an energy range of 10 eV, with a reciprocal space step of 0.01 $Å^{-1}$.

As a result of the performed calculations, two electronic band structure diagrams were obtained: one without SOC, as shown in Figure S5(a), and one with SOC, as shown in Figure S5(b).). These diagrams illustrate the effect of SOC on the band dispersion. The band structures are presented along high-symmetry directions in the Brillouin zone, as defined by the crystal symmetry. The most relevant region of the band structure diagrams lies near the direct optical transition at the Γ-point. It can be seen that the spin-split states of the light and heavy electrons shift to higher energies when spin-orbit coupling is taken into account.

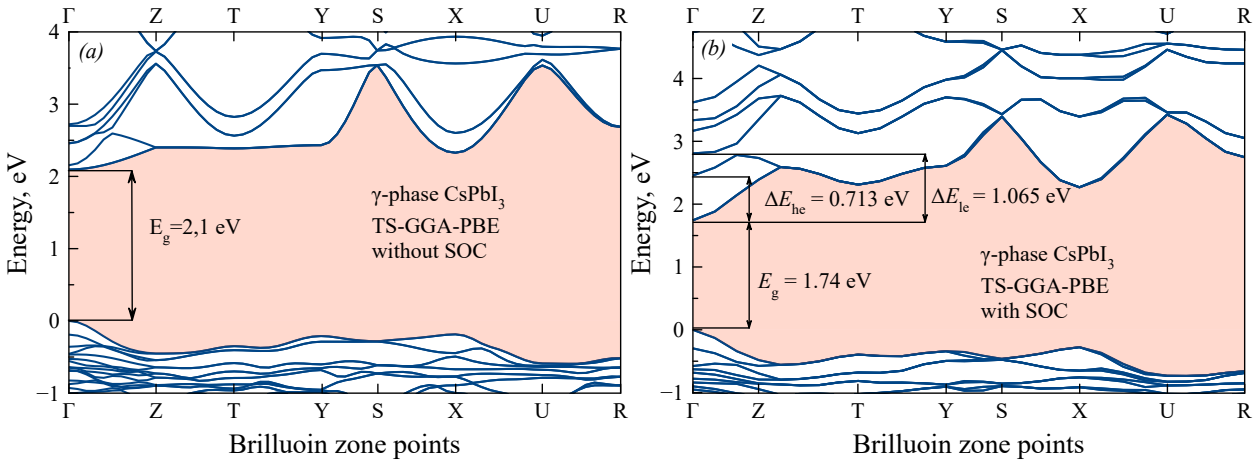

Figure S5: The band structure of $CsPbI_3$ perovskite calculated for the γ-phase orthorhombic modification: (a) without SOC and (b) with SOC.

Figure S5 (b) presents the corresponding splitting values for the light ($\Delta E_{\text{he}} = 0.713$ eV) and heavy ($\Delta E_{\text{le}} = 1.065$ eV) electron states. Taking into account the value of the band gap $E_{\text{g}} = 1.71$ eV, the calculated energies of the spin-split states are found to be close to the energy of the feature observed in the two-photon excitation spectrum at 2.6 eV.

References

(1) Kuznetsova, M. S.; Kolobkova, E. V.; Bataev, M. N.; Berdnikov, V. S.; Pankin, D. V.; Smirnov, M. B.; Ubyivovk, E. V.; Ignatiev, I. V. Synthesis and optical properties of perovskite nanocrystals in glass with cationic substitution. The Journal of Chemical Physics **2024**, 161, 124501.

(2) Kirstein, E.; Kopteva, N. E.; Yakovlev, D. R.; Zhukov, E. A.; Kolobkova, E. V.; Kuznetsova, M. S.; Belykh, V. V.; Yugova, I. A.; Glazov, M. M.; Bayer, M.; Greilich, A. Mode locking of hole spin coherences in $CsPb(Cl,Br)_3$ perovskite nanocrystals. Nat. Commun. **2023**, 14, 699.

(3) Kulebyakina, E. V.; Skorikov, M. L.; Kolobkova, E. V.; Kuznetsova, M. S.; Bataev, M. N.; Yakovlev, D. R.; Belykh, V. V. Temperature-dependent photolumi-

nescence dynamics of $CsPbBr_3$ and $CsPb(Cl,Br)_3$ perovskite nanocrystals in a glass matrix. Phys. Rev. B **2024**, 109, 235301.

(4) Nie, Z.; Shi, G.; Li, Z.; Wang, Y.; Zhang, X.; Shui, M.; Ao, G.; Yang, J.; Song, Y. Measurement of nonlinear refraction of thick samples using nonlinear-imaging technique with a phase object. Optics & Laser Technology **2014**, 59, 36–42.

(5) Jin, M.; Liang, X.; Zhang, H.; Liu, J.; Shao, G.; Xiang, W.; Song, Y. A promising optical limiting material: Tunable third-order nonlinear optical properties of robust CsPbX3 (X=Cl/Br, Br) nanocrystals glasses. Journal of the European Ceramic Society **2020**, 40, 4140–4147.

(6) He, C.; Fan, J.; Li, Z.; Gao, Y.; Chen, Z.; Song, Y.; Wu, Y.; wang, B. Self-assembled multilayer films containing 1,8,15,22-tetrakis (8-quinolineoxy-5-sulfonic acid)-phthalocyanine copper: Preparation, and third order nonlinear optical properties. Optical Materials **2014**, 36, 746–752.

(7) Zheng, X.; Chen, R.; Shi, G.; Zhang, J.; Xu, Z.; Cheng, X.; Jiang, T. Characterization of nonlinear properties of black phosphorus nanoplatelets with femtosecond pulsed Z-scan measurements. Opt. Lett. **2015**, 40, 3480–3483.

(8) Ajami, A.; Husinsky, W.; Liska, R.; Pucher, N. Two-photon absorption cross section measurements of various two-photon initiators for ultrashort laser radiation applying the Z-scan technique. J. Opt. Soc. Am. B **2010**, 27, 2290–2297.

(9) Gu, B.; Wang, J.; Chen, J.; Fan, Y.-X.; Ding, J.; Wang, H.-T. Z-scan theory for material with two- and three-photon absorption. Opt. Express **2005**, 13, 9230–9234.

(10) Chen, J.; Zhang, W.; Pullerits, T. Two-photon absorption in halide perovskites and their applications. Mater. Horiz. **2022**, 9, 2255–2287.

(11) Xu, Z.; Chen, T.; Zhang, D.; Zheng, G.; Wu, J.; Yan, J.; Liu, X.; Qiu, J. Linear and nonlinear optical characteristics of $CsPbBr_3$ perovskite quantum dots-doped borosilicate glasses. J. Eur. Ceram. Soc. **2021**, 41, 729–734.

(12) Wang, Y.; Li, X.; Zhao, X.; Xiao, L.; Zeng, H.; Sun, H. Nonlinear Absorption and Low-Threshold Multiphoton Pumped Stimulated Emission from All-Inorganic Perovskite Nanocrystals. Nano Lett. **2016**, 16, 448–453, PMID: 26652773.

(13) Wei, K.; Xu, Z.; Chen, R.; Zheng, X.; Cheng, X.; Jiang, T. Temperature-dependent excitonic photoluminescence excited by two-photon absorption in perovskite CsPbBr3 quantum dots. Opt. Lett. **2016**, 41, 3821–3824.

(14) Lu, W.-G.; Chen, C.; Han, D.; Yao, L.; Han, J.; Zhong, H.; Wang, Y. Nonlinear optical properties of colloidal CH3NH3PbBr3 and CsPbBr3 quantum dots: a comparison study using Z-scan technique. Advanced Optical Materials **2016**, 4, 1732–1737.

(15) Liu, S.; Chen, G.; Huang, Y.; Lin, S.; Zhang, Y.; He, M.; Xiang, W.; Liang, X. Tunable fluorescence and optical nonlinearities of all inorganic colloidal cesium lead halide perovskite nanocrystals. Journal of Alloys and Compounds **2017**, 724, 889–896.

(16) Ketavath, R.; Katturi, N. K.; Ghugal, S. G.; Kolli, H. K.; Swetha, T.; Soma, V. R.; Murali, B. Deciphering the Ultrafast Nonlinear Optical Properties and Dynamics of Pristine and Ni-Doped CsPbBr3 Colloidal Two-Dimensional Nanocrystals. The Journal of Physical Chemistry Letters **2019**, 10, 5577–5584, PMID: 31468971.

(17) Krishnakanth, K. N.; Seth, S.; Samanta, A.; Rao, S. V. Broadband femtosecond nonlinear optical properties of CsPbBr3 perovskite nanocrystals. Optics Letters **2018**, 43, 603–606.

(18) Zhao, F.; Li, J.; Gao, X.; Qiu, X.; Lin, X.; He, T.; Chen, R. Comparison Studies of the Linear and Nonlinear Optical Properties of CsPbBrxI3–x Nanocrystals: The Influence

of Dimensionality and Composition. The Journal of Physical Chemistry C **2019**, 123, 9538–9543.

(19) Clark, S.; Segall, M.; Pickard, C.; Hasnip, P.; Probert, M.; Refson, K.; Payne, M. First principles methods using CASTEP. Zeitschrift für Kristallographie **2005**, 220, 567–570, Reproduced with permission from the publisher.

(20) Tkatchenko, A.; Scheffler, M. Accurate molecular van der Waals interactions from ground-state electron density and free-atom reference data. Phys Rev Lett **2009**, 102, 073005.

(21) Refson, K.; Tulip, P. R.; Clark, S. J. Variational density-functional perturbation theory for dielectrics and lattice dynamics. Phys. Rev. B **2006**, 73, 155114.

(22) Aarons, J. A new CASTEP and ONTEP geometry optimiser. **2011**,

(23) Byrd, R. H.; Nocedal, J.; Schnabel, R. B. Representations of quasi-Newton matrices and their use in limited memory methods. Mathematical Programming **1994**, 63, 129–156.

(24) Monkhorst, H. J.; Pack, J. D. Special points for Brillouin-zone integrations. Phys. Rev. B **1976**, 13, 5188–5192.